Processes determining the marine alkalinity and calcium carbonate saturation distributions

Carter, B. R.[1], J. R. Toggweiler[2], R. M. Key[1], and J. L. Sarmiento[1]

Brendan Carter (brcarter@princeton.edu

J.R. Toggweiler (Robbie.Toggweiler@noaa.gov)

Robert M. Key (key@princeton.edu)

Jorge L. Sarmiento (jls@princeton.edu)

[1] Atmospheric and Oceanic Sciences Program, Princeton University, Princeton, NJ, USA
[2] Geophysical Fluid Dynamics Laboratory, National Oceanic and Atmospheric Administration, P.O. Box 308, Princeton NJ, 08542, USA

Abstract

We introduce a composite tracer, *Alk**, that has a global distribution primarily determined by $CaCO_3$ precipitation and dissolution. *Alk** is also affected by riverine alkalinity from dissolved terrestrial carbonate minerals. We estimate the Arctic receives approximately twice the riverine alkalinity per unit area as the Atlantic, and 8 times that of the other oceans. Riverine inputs broadly elevate *Alk** in the Arctic surface and particularly near river mouths. Strong net carbonate precipitation results in low *Alk** in subtropical gyres, especially in the Indian and Atlantic Oceans. Upwelling of dissolved $CaCO_3$ rich deep water elevates Northern Pacific and Southern Ocean *Alk**. We use the *Alk** distribution to estimate the calcite saturation variability resulting from $CaCO_3$ cycling and other processes. We show regional differences in surface calcite saturation are due to the effect of temperature differences on CO_2 solubility and, to a lesser extent, differences in freshwater content and air-sea disequilibria. The variations in net calcium carbonate cycling revealed by *Alk** play a comparatively minor role.

1. Introduction

Our goal is to use high-quality total alkalinity (A_T) observations to examine the effects of calcium carbonate cycling on marine A_T and calcium carbonate saturation states. This study is motivated in part by ocean acidification. With marine calcite saturation decreasing due to anthropogenic carbon uptake, it is important to understand the degree to which carbonate cycling impacts calcite saturations.

Marine calcium carbonate cycling includes both internal and external calcium carbonate cycling. Internal cycling refers to net formation of $67\text{-}300 \times 10$ Tmoles A_T yr^{-1} worth of calcium carbonate (Berelson et al., 2007) in the surface ocean and net dissolution of most of this calcium

carbonate at depth. External marine carbonate cycling refers to inputs of carbonate minerals dissolved in rivers, sediment pore waters, hydrothermal vent fluids, and submarine groundwater discharge, and loss due to biogenic carbonate mineral burial and authigenic mineralization in sediments. Rivers add 33 Tmoles A_T yr^{-1} worth of dissolved bicarbonate to the ocean (Cai et al., 2008). Wolery and Sleep (1988) estimate hydrothermal vents add an additional 6.6 Tmoles A_T yr^{-1}, though deVilliers (1998) argues the hydrothermal contribution may be as high as 30 Tmoles A_T yr^{-1}. Submarine groundwater discharge is poorly constrained, but is thought to exceed riverine inputs in some areas (Moore, 2010).

We investigate calcium carbonate cycling using the global A_T distribution in a dataset we created by merging the PACIFICA (Suzuki et al., 2013), GLODAP, and CARINA discrete data products (Key et al. 2004; 2010; Velo et al., 2009). We have combined and gridded these data products using methods detailed in Supplementary Materials document SA. We use our gridded dataset in some calculations to limit sampling biases and to enable us to make volume-weighted mean property estimates.

Dickson (1981) defines total alkalinity as the concentration excess "of proton acceptors formed from weak acids ($pK \leq 4.5$) relative to proton donors (weak bases with $pK > 4.5$)" at a reference temperature, pressure, and ionic strength. A_T can be thought of as a measure of how well buffered seawater is against changes in pH. This operational definition gives A_T (expressed in mol kg^{-1}) several properties that make it an especially useful carbonate system parameter for examining carbonate cycling:

1. It mixes conservatively,
2. … and is therefore diluted and concentrated linearly by evaporation and precipitation.
3. It responds in predictable ways to calcium carbonate cycling.

4. … as well as organic matter formation and remineralization.
5. It is not changed by air-sea exchange of heat or carbon dioxide.
6. It is however affected by anaerobic redox reactions (Chen, 2002).

We are primarily interested calcium carbonate cycling, item 3 in our list. In section 2 of this paper we therefore define a tracer we call *Alk** that removes the majority of the influences of organic matter cycling (item 4), freshwater cycling (item 2), and non-sedimentary anaerobic redox reactions (item 6) while still mixing conservatively, remaining insensitive to gas exchange, and responding to calcium carbonate cycling. In section 3 we discuss processes that govern the *Alk** distribution globally, by ocean basin, and regionally. In section 4 we define a metric to quantify the influence of various processes on the marine calcite saturation state. We use this metric with our gridded dataset and *Alk** to determine the relative importance of the various controls on calcite saturation in the ocean and at the ocean surface. We summarize our findings in section 5.

2. The *Alk** tracer

In defining *Alk**, we take advantage of the potential alkalinity (Brewer et al., 1975) concept to remove the majority of the influence of organic matter cycling and denitrification, and use a specific salinity normalization scheme (Robbins, 2001) to remove the influence of freshwater cycling. We detail the *Alk** definition and the reasoning behind it in this section.

The influence of organic matter cycling on A_T is due primarily to the biologically-driven marine nitrogen cycle. Nitrate uptake for anaerobic denitrification and the production of amino acids occurs in an ~1:1 mole ratio with the release of molecules that increase A_T (Chen, 2002). Similarly, nitrate from fixation of nitrogen gas and remineralization of amino nitrogen is released

in a 1:1 mole ratio with acids that titrate away A_T (Wolf-Gladrow et al., 2007). This observation led Brewer et al. (1975) to propose the idea of "potential alkalinity" as the sum of A_T and nitrate with the aim of creating a tracer that responds to the cycling of calcium carbonates without changing in response to organic matter cycling. Feely et al. (2002) since used a variant that relies on the empirical relationship between dissolved calcium concentrations, A_T, and nitrate determined by Kanamori and Ikegami (1982). This variant has the advantage of implicitly accounting for the A_T changes created by the exchange of numerous other components of marine organic matter besides nitrate (e.g. sulfate and phosphate). We thus use the ratio found by Kanamori and Ikegami (1982) to define potential alkalinity (A_P).

$$A_P = A_T + 1.26 * [NO_3^-] \quad (1)$$

While the empirical ratio of 1.26 may be specific to the elemental ratios of the North Pacific, Wolf-Gladrow et al. (2007) provide a theoretical derivation from Redfield ratios and obtain a similar value of 1.36.

The sensitivity of the A_T distribution to freshwater cycling is due primarily to the dilution or concentration of the large background A_T fraction that does not participate in carbonate cycling on timescales of ocean mixing. This background fraction behaves conservatively, so we call it conservative potential alkalinity (A_P^C) and estimate it directly from salinity as:

$$A_P^C \equiv S \frac{\overline{A_P}}{\overline{S}} \quad (2)$$

Here, terms with a bar are reference values chosen as the mean value for those properties in the top 20 meters of the ocean. We obtain a volume-weighted surface $\overline{A_P}$ (2305 µmol kg^{-1}) to $\overline{S}$ (34.71) ratio of 66.40 µmol kg^{-1} from our gridded dataset. The mean surface values are chosen in an effort to best capture the impact of freshwater cycling where precipitation and evaporation

92 occur.

93 Robbins (2001) showed that subtracting an estimate of the conservative portion of a
94 tracer, such as A_P^C, produces a salinity-normalized composite tracer that mixes conservatively.
95 This scheme also retains the 2:1 change of A_T to dissolved inorganic carbon (C_T) with carbonate
96 cycling. We follow this approach in our definition of *Alk**. In Supplementary Materials
97 document SB we estimate this approach removes 97.5% of the influence of freshwater cycling
98 on potential alkalinity and reduces the influence of freshwater cycling on *Alk** to less than 1% of
99 the *Alk** variability. In Supplementary Materials document SC we demonstrate that *Alk** mixes
100 conservatively, and briefly contrast *Alk** to traditionally normalized potential alkalinity which
101 does not mix conservatively (Jiang et al., 2014).

102 In total, we define *Alk** as the deviation of potential alkalinity from A_P^C,

$$Alk^* \equiv A_P - A_P^C \tag{3}$$

103
$$\equiv A_P - \frac{\overline{A_P}}{\overline{S}} S \tag{4}$$

$$\equiv A_P - 66.4 \times S \tag{5}$$

104 where *Alk** has the same units as A_T (μmol kg^{-1}). The *Alk** distribution is attributable primarily
105 to carbonate cycling plus the small residual variation due to freshwater cycling that is not
106 removed by subtracting A_P^C. However, hydrothermal vent fluid and non-denitrification
107 anaerobic redox chemistry may substantively affect alkalinity distributions in certain marine
108 environments, and *Alk** distributions could not be attributed purely to internal and external
109 calcium carbonate cycling in these locations.

110 Mean global surface *Alk** is zero by definition, and thus *Alk** can have negative as well
111 as positive values. For reference, more than 95% of our gridded *Alk** dataset falls between –35
112 and 220 μmol kg^{-1}.

3. *Alk** distributions

We consider *Alk** distributions globally, by ocean basin, and regionally in the context of sources and sinks of the tracer both globally and regionally. We pay special attention to riverine *Alk** because it is easily identified where it accumulates near river mouths.

*3.1 Global distribution of Alk**

Figure 1 maps surface *Alk** (top 50 m) at the measurement stations. We provide this figure to show where we have viable *Alk** estimates and to demonstrate that our gridded data product adequately captures the measured *Alk** distribution. Figure 2 maps gridded global surface A_T, salinity, *Alk**, and phosphate distributions and mask the regions that are lacking data in Fig. 1.

The similarity of the A_T (Fig. 2a) and salinity (Fig. 2b) distributions demonstrates the strong influence of freshwater cycling on the surface marine A_T distribution (see also: Millero et al. 1998, Jiang et al., 2014). The dissimilarity between *Alk** (Fig. 2c) and salinity (Fig. 2b) suggests *Alk** removes the majority of this influence. The phosphate (Fig. 2d) and *Alk** (Fig. 2c) distributions are similar at the surface. They are also similar at depth: Figures 3 and 4 show zonally-averaged gridded depth sections of *Alk** and phosphate. *Alk** and phosphate concentrations are low in the deep Arctic Ocean (Figs. 3d, and 4d), intermediate in the deep Atlantic Ocean (Figs. 3a and 4a), and high in the deep North Pacific (Figs. 3b and 4b) and deep North Indian (Figs. 3c and 4c) Oceans. *Alk** and phosphate distributions are similar because similar processes shape them: the hard and soft tissue pumps transport A_T and phosphate, respectively, from the surface to depth. The "oldest" water therefore has the highest net

phosphate and *Alk** accumulation. High surface phosphate and *Alk** in the Southern Ocean and North Pacific in Figs. 2, 3, and 4 are due to upwelled old deep waters.

Several qualitative differences between *Alk** and phosphate distributions are visible in Figs. 2c, 2d, 3, and 4. Surface phosphate is low in the Bay of Bengal and high in the Arabian Sea (Fig. 2d), while the opposite is true for *Alk** (Fig. 2c). Also, *Alk** reaches its highest surface concentration in the Arctic (Figs. 2c and 3d) where phosphate is not greatly elevated (Figs. 2d and 4d). These surface differences are due to regional riverine *Alk** inputs (Section 3.3). Another difference is that *Alk** reaches a maximum below 2000 m in all ocean basins except the Arctic, while phosphate maxima are above 2000 m. We attribute the deeper *Alk** maxima to deeper dissolution of calcium carbonates than organic matter remineralization. Finally, *Alk** values are higher in the deep Indian Ocean than in the deep Pacific. This is likely due to elevated biogenic carbonate export along the coast of Africa and in the Arabian Sea (Sarmiento et al., 2002; Honjo et al., 2008).

3.2 Alk by ocean basin*

In Fig. 5 we provide 2-D color histograms of discrete surface *Alk** and salinity measurements for the five major ocean basins. Figure 5 also provides volume-weighted mean gridded Alk* for each basin. We attribute the decrease in *Alk** as salinity increases—especially visible in the low-salinity bins in the Arctic Ocean (Fig. 5d)—to mixing between high-*Alk** low-salinity river water and low-*Alk** high-salinity open ocean water. Net precipitation in the tropics and net evaporation in the subtropics widens the histograms across a range of salinities and alkalinities without affecting *Alk** in Figs. 5a, 5b, and 5c. The *Alk** elevation associated with upwelled water is most visible in Fig. 5e where Upper Circumpolar Deep Water upwelling near

the Polar Front results in high-frequency (i.e. warm colored) histogram bins at high-*Alk**. Similarly, the high-frequency *Alk** bins in Fig. 5b with salinity between 32.5 and 33.5 are from the North Pacific Subpolar Gyre, and are due to upwelled old high-*Alk** water (cf. the Si* tracer in Sarmiento et al. (2004)). River water contributions can be most easily seen in a scattering of low-frequency (cool colored) high-*Alk** and low-salinity bins in the Arctic Ocean.

The surface Southern Ocean has the highest *Alk** followed by the Arctic, Pacific, and the Indian and Atlantic. The high mean Southern Ocean *Alk** is due to upwelling. The high mean Arctic surface *Alk** is due to riverine input. The Atlantic and the Arctic together receive ~65% of all river water (Dai and Trenberth, 2002). We construct a budget for terrestrial A_T sources to the various surface ocean basins using the following assumptions:

1. the A_T of 25 large rivers are as given by Cai et al. (2008),
2. the volume discharge rates of 200 large rivers are as given by Dai and Trenberth (2002),
3. groundwater and runoff enter each ocean in the same proportion as river water from these 200 rivers,
4. the A_T of all water types that we do not know from assumption 1. is the 1100 μmol kg^{-1} global mean value estimated by Cai et al. (2008), and
5. 40°N is the boundary between the Atlantic and the Arctic and 40°S is the boundary between the Southern and the Atlantic Oceans (based upon the region of elevated surface phosphate in Fig. 2d),

Our detailed budget is provided as Supplementary Materials file SD. We estimate 40% of continentally derived A_T enters the Atlantic, 20% enters the Arctic, and 40% enters all remaining ocean basins. These ocean areas represent 17%, 5%, and 78% of the total surface ocean area in

our gridded dataset respectively, so the Artic receives approximately twice as much riverine A_T per unit area as the Atlantic, and 8 times the rest of the world ocean. The Atlantic has the lowest open-ocean surface *Alk** value and the lowest basin mean surface *Alk** despite the large riverine sources. The large riverine A_T input must therefore be more than balanced by strong net calcium carbonate formation. The Indian Ocean has comparably low mean surface *Alk** to the Atlantic, but a smaller riverine source. Mean *Alk** is higher in the Pacific than the Atlantic and Indian, even when neglecting the upwelling region north of 40°N (*Alk** = −16.5 μmol kg^{-1} when omitted). Considering the weak Pacific riverine input, this suggests that, relative to other ocean basins, there are either larger *Alk** inputs from exchange with other basins and deeper waters or smaller Pacific basin mean net calcium carbonate.

3.3 Riverine Alk regionally*

For river water with negligible salinity, *Alk** equals the potential alkalinity. This averages around 1100 μmol kg^{-1} globally (Cai et al., 2008), but is greater than 3000 μmol kg^{-1} for some rivers (Beldowski et al., 2010). Evidence suggests that riverine A_T is increasing due to human activities (Kaushal et al., 2013).

The most visible riverine *Alk** signals are in the Arctic due to the large riverine runoff into this comparatively small basin and the confinement of this low-density riverine water to the surface (Jones et al., 2008; Yamamoto-Kawai et al., 2009; Azetsu-Scott et al., 2010). Figure 4d shows the high Arctic *Alk** plume is confined to the top ~200 m. Figure 3 shows that these high *Alk** values extend along the coast of Greenland and through the Labrador Sea. *Alk** decreases with increasing salinity in this region (Fig. 6d) due to mixing between the fresh high *Alk** surface Arctic waters and the salty lower *Alk** waters of the surface Atlantic. Gascard et al. (2004a, b)

suggest that high *Alk** waters along the coast of Norway are part of the Norwegian Coastal Current, and originate in the Baltic and North Seas where there are also strong riverine inputs (Thomas et al., 2005).

Elevated *Alk** can also be seen in the Bay of Bengal with surface values ~100 μmol kg^{-1} higher than those in the central Indian Ocean. This bay has two high A_T rivers that join and flow into it, the Brahmaputra (A_T = 1114 μmol kg^{-1}) and the Ganges (A_T = 1966 μmol kg^{-1}) (Cai et al., 2008). Figure 7 provides *Alk** depth sections for both areas. The riverine *Alk** plume can be clearly seen in the top 50 m of the Bay of Bengal. No similar increase is seen in the Arabian Sea where the Indus River (1681 μmol kg^{-1}) discharges only ~1/10th of the combined volume of the Brahmaputra and the Ganges.

The Amazon River is the largest single riverine marine A_T source. This river has low A_T (369 μmol kg^{-1} (Cai et al., 2008)), but has the largest water discharge volume of any river, exceeding the second largest—the Congo—by a factor of ~5 (Dai and Trenberth, 2002). Consequently, the Amazon discharges approximately 50% more A_T per year than the river with the second largest A_T discharge, the Changjiang (Cai et al., 2008). The Amazon's influence can be seen as a region of abnormally low salinity and A_T in Fig. 2a and b. Despite the high discharge volume, the influence is only barely visible as a region of elevated *Alk** in Fig. 2c due to the comparatively low Amazon *Alk**. However, the influence of the Amazon on *Alk** can be seen in the seasonal *Alk** cycle in the Amazon plume. Figure 7 provides a map of *Alk** for this region scaled to show the influence of this low *Alk** river in the Northern Hemisphere (a) winter and (b) summer months. The higher *Alk** found for summer months is consistent with Amazon discharge and A_T seasonality (Cooley et al., 2007) and Moore et al.'s (1986) radium isotope based finding that Amazon River outflow comprises 20-34% of surface water in this region in

July compared to only 5-9% in December.

3.4 Regional inorganic carbonate cycling

The Red Sea portion of Fig. 8 is strongly depleted in *Alk**, and contains the lowest single *Alk** measurement in our dataset, –247 μmol kg^{-1}. The GEOSECS expedition Red Sea alkalinity measurements (Craig and Turekian, 1980) predate alkalinity reference materials (Dickson et al., 2007), but are supported by more recent measurements (Silverman et al., 2007). Like Jiang et al. (2014), we attribute low Red Sea *Alk** to exceptionally active calcium carbonate formation.

The Red Sea is one of the only regions where calcium carbonate saturation is sufficiently high for inorganic carbonate precipitation to significantly contribute to overall carbonate precipitation (Milliman et al. 1969; Silverman et al., 2007). Notably, saturation remains high at depth in the Red Sea (see Section 4.2). Despite this, carbonate sediments in the modern Red Sea are mostly biogenic aragonitic corals and pteropod shells (Gevirtz and Friedman, 1966). However, in this region, pores in sediments are filled in with high-magnesium calcite cement (Almogi-Labin et al., 1986). We hypothesize biogenic carbonates are dissolved by CO_2 from sedimentary organic matter remineralization, as occurs elsewhere (e.g. Hales and Emerson, 1997; Hales, 2003; Boudreau, 2013), but that high deep Red Sea calcium carbonate saturation leads to inorganic re-calcification in sediment pores.

Inorganic calcium carbonate has recently been found as metastable ikaite (a hydrated calcium carbonate mineral with the formula $CaCO_3 \cdot 6H_2O$) in natural sea ice (Dieckmann et al., 2008). Ikaite cycling provides a competing explanation for the high Arctic surface *Alk** values if high A_T low-salinity ikaite-rich ice melt becomes separated from low A_T high-salinity rejected

brines. However, riverine A_T inputs better explain the magnitude of the feature: The ~5 mg ikaite L^{-1} sea ice Dieckmann et al. (2008) found in the Antarctic could only enrich A_T of the surface 100 m by ~1 µmol kg^{-1} for each meter of ice melted, and Arctic surface 100 m *Alk** is elevated by 59 µmol kg^{-1} relative to the deeper Arctic in our gridded dataset. By contrast, Jones et al. (2008) estimate a ~5% average riverine end-member contribution to the shallowest 100 m of this region, which accounts for ~55 µmol kg^{-1} *Alk** enrichment. Also, surface *Alk** in the Southern Ocean—which has sea ice but lacks major rivers—is not similarly elevated relative to phosphate (Fig. 2) or deep *Alk** (Fig. 3).

4. Controls on the calcite saturation state

The *Alk** tracer provides an opportunity to estimate the impact of carbonate cycling on the calcite saturation. In addition to (1) carbonate cycling, calcite saturation is affected by (2) organic matter cycling, (3) freshwater cycling, (4) pressure changes on seawater, (5) heating and cooling, and (6) A_T changes from nitrogen fixation and denitrification. For each of these six processes, we estimate the standard deviation of the net influence of the process globally by considering the standard deviation of a "reference" tracer R_i for the process, "σ_{R_i}", where R_i is *Alk** for $CaCO_3$ cycling, phosphate for organic matter cycling, salinity for freshwater cycling, pressure for pressure changes, temperature for heating and cooling, and *N** (Gruber and Sarmiento, 1997) for nitrogen fixation and denitrification. We use the standard deviation of the reference tracer as a measure of the oceanic range of the net influence of the corresponding process. We measure the impact of this range on calcite saturation using a metric *M*, which we define as:

$$M_i = \sigma_{R_i} \left| S_{R_i} \right| \quad (6)$$

where S_{R_i} is the calcite saturation sensitivity to a unit process change in R_i, which we estimate in Appendix A. We are interested in the relative importance *I* of our 6 processes, so we also calculate the percentage that each metric value estimate contributes to the sum of all 6 metric value estimates:

$$I_i = 100\% \times \frac{M_i}{\sum_{i=1}^{6} M_i} \quad (7)$$

We derive and estimate our metric and its uncertainty in Appendix A. We carry out our analysis for the full water column assuming it to be isolated from the atmosphere (section 4.1), and also for just the top 50 m of the water column assuming it to be well-equilibrated with the atmosphere (section 4.2). Finally, we consider how equilibration with an atmosphere with a changing pCO_2 alters surface calcite saturation.

4.1 Process importance in atmospherically-isolated mean seawater from all ocean depths

Our metric M_i is an estimate of the standard deviation of the global distribution of Ω_C resulting from the *i*th process. Our relative process importance metric I_i is an estimate of the percentage of overall variability of the Ω_C distribution that can be attributed to that process. We provide *M* and *I* values for mean seawater from the full water column alongside the R_i, S_{R_i}, and σ_{R_i} values used to estimate them in Table 1. These calculations assume that the seawater is isolated from the atmosphere.

Relative process importance estimates *I* indicate organic matter cycling (48%) is the dominant process controlling calcite saturation for mean seawater. Changing pressure (28%) is the second most important process, followed by calcium carbonate cycling (17%), temperature

changes (4%), nitrogen fixation and denitrification (1.21%), and freshwater cycling (0.78%).

4.2 Process importance in well-equilibrated surface seawater

In Table 2 we provide M_i values for well-equilibrated seawater in the top 50 m of the ocean alongside the R_i, σ_{R_i}, S_{R_i} used to estimate them. These surface seawater M_i values are calculated assuming the water remains equilibrated with an atmosphere with 400 µatm pCO$_2$. We test the validity of this assumption by also estimating M for the observed global pCO$_2$ variability in the Takahashi et al. (2009) global data product. This test reveals transient air-sea disequilibria are indeed important for surface ocean calcite saturation, but only as a secondary factor when considered globally. Despite this, it is important to recognize that air-sea equilibration following a process is not instantaneous, and that the S_{R_i} value estimates in section 4.1 will be better for estimating short term changes following fast acting processes such as spring blooms (e.g. Tynan et al., 2014) or upwelling events (e.g. Feely et al., 1988). We omit the disequilibrium M value estimate from the denominator of Eq. (7) to allow I values for surface seawater to be compared to I values from mean seawater globally.

Warming and cooling are the dominant processes controlling Ω_C for well-equilibrated surface seawater (76%). The large increase in M for warming and cooling relative to the value calculated for mean seawater is due to lower equilibrium C_T at higher temperatures. Freshwater cycling is the second most important process (13%), followed by carbonate cycling (8%), organic matter cycling (2%), pressure changes (1%), and denitrification and nitrogen fixation (0.4%). The increased importance of freshwater cycling is because freshwater dilutes C_T by more than the equilibrium C_T decreases from A_T dilution, so carbon uptake tends to follow freshwater precipitation and carbon outgassing follows evaporation. Carbonate cycling is less

318 important because A_T decreases with carbonate precipitation lead to lower C_T at equilibrium.
319 Organic matter cycling is much less important because atmospheric re-equilibration mostly
320 negates the large changes in C_T. Pressure changes are negligible because we only consider water
321 in the surface 50 m. Our air-sea disequilibrium *M* estimate suggests surface disequilibria are
322 comparably important to freshwater cycling for surface calcite saturation, but substantially less
323 important than temperature changes (this would correspond to an *I* value of ~14%).

324 The dominance of warming and cooling and freshwater cycling over carbonate cycling is
325 most evident in the Red Sea where high temperatures (>25 °C) and high salinities (>40) lead to
326 surface calcite saturations exceeding 6 despite extremely low *Alk** (<–200 μmol kg^{-1}). The deep
327 Red Sea is also unusual for having deep water that was warm when it last left contact with the
328 atmosphere (the Red Sea is >20 °C at >1000 m depth). This provides high initial deep calcite
329 saturation that—combined with decreased influence of pressure changes at higher
330 temperatures—keeps deep Red Sea $\Omega_C > 3$. Similarly, the lowest surface saturation states are in
331 the Arctic where there are low temperatures, low salinity, and high *Alk** from riverine inputs.
332 The importance of warming and cooling is also suggested by the correlation between global
333 surface calcite saturation and the surface temperature ($R^2 = 0.96$) shown for our gridded dataset
334 in Fig. 8.
335
336 **5. Conclusions**
337 *Alk** isolates the portion of the A_T signal that varies in response to calcium carbonate
338 cycling and exchanges with terrestrial and sedimentary environments from the portion that varies
339 in response to freshwater and organic matter cycling. The salinity normalization we use has the
340 advantage over previous salinity normalizations that it allows our tracer to mix linearly and

change in a 2:1 ratio with C_T in response to carbonate cycling. We highlight the following insights from *Alk**:

(1) Alk distribution*: The *Alk** distribution clearly shows the influence of biological cycling including such features as the very low *Alk** in the Red Sea due to the high calcium carbonate precipitation there. We also find evidence of strong riverine A_T sources in the Bay of Bengal and in the Arctic. We show river inputs likely dominate over the small influences of ikaite cycling on the Arctic alkalinity distribution.

(2) Influence of calcium carbonate cycling on marine calcite saturation: *Alk** allows us to quantify the net influence of calcium carbonate cycling on marine calcite saturation. For well-equilibrated surface waters, carbonate cycling is less influential for calcite saturation than gas exchange driven by warming and cooling and freshwater cycling. At depth, the carbonate cycling signal is smaller than the signal from organic matter cycling and from pressure changes. Temperature is the dominant control on calcite saturation of surface waters in equilibrium with the atmosphere. This accounts for the low calcite saturation states in the cold surface of the Arctic and Southern Oceans despite high regional *Alk**, and high calcite saturations in the warm subtropics despite low regional *Alk**.

We intend to use *Alk** for two future projects. First, *Alk** is superior to A_T for monitoring and modeling changes in marine chemistry resulting from changes in carbonate cycling with ocean acidification. A_T varies substantially in response to freshwater cycling, so *Alk** trends may be able to be detected sooner and more confidently attributed to changes in calcium carbonate cycling than trends in A_T. Preliminary explorations of Earth System Model output suggest time of trend emergence for the alkalinity trends discussed by Ilyina et al. (2009) could be reduced by as much as a factor of 5. Secondly, we will estimate global steady state *Alk** distributions using

364 *Alk** sources and sinks from varied biogeochemical ocean circulation models alongside
365 independent water mixing and transport estimates (e.g. Khatiwala et al., 2005; Khatiwala, 2007).
366 We will interpret findings in the context of two hypotheses proposed to explain evidence for
367 calcium carbonate dissolution above the aragonite saturation horizon: (1) that organic matter
368 remineralization creates undersaturated microenvironments that promote carbonate dissolution in
369 portions of the water column which are chemically supersaturated in bulk, and (2) that high-
370 magnesium calcite and other impure minerals allow chemical dissolution above the saturation
371 horizon.
372
373 **Acknowledgements**

374 We thank Eun Young Kwon for contributions to early versions of this research. We also
375 thank the US National Science Foundation for research support (ANT-1040957), as well as the
376 numerous scientists and crew that contributed to the datasets used in this study. R. Key was
377 supported by CICS grant NA08OAR432052. We also thank anonymous reviewers for their
378 helpful and constructive comments.
379
380 **References**

381 Almogi-Labin, A., B. Luz, and J. Duplessy (1986), Quaternary paleo-oceanography, pteropod
382 preservation and stable-isotope record of the Red Sea, *Palaeogeogr., Palaeoclimateol.,*
383 *Palaeoecol.*, *57*, 195-211, DOI: 10.1016/0031-0182(86)90013-1.
384 Anderson, L. A. and J. L. Sarmiento (1994), Redfield ratios of remineralization determined by
385 nutrient data analysis, *Global Biogeochem. Cycles, 8*, 65-80, doi: 10.1029/93GB03318.
386 Azetsu-Scott, K., A. Clarke, K. Falkner, J. Hamilton, E. P. Jones, C. Lee, B. Petrie, S.

Prinsenberg, M. Starr, and P. Yeats (2010), Calcium carbonate saturation states in the waters of the Canadian Arctic Archipelago and the Labrador Sea, *J. Geophys. Res. Oceans, 115*, C11.

Beldowski, J., A. Löffler, B. Schneider, and L. Joensuu (2010), Distribution and biogeochemical control of total CO_2 and total alkalinity in the Baltic Sea, *J. Mar. Sys., 81*, 252-259.

Berelson, W. M., W. M. Balch, R. Najjar, R. A. Feely, C. Sabine, and K. Lee (2007), Relating estimates of $CaCO_3$ production, export, and dissolution in the water column to measurements of $CaCO_3$ rain into sediment traps and dissolution on the sea floor: A revised global carbonate budget, *Global Biogeochem. Cycles, 21*, GB1024, doi: 10.1029/2006GB002803.

Boudreau, B. P. (2013), Carbonate dissolution rates at the deep ocean floor, *Geophys. Res. Lett., 40*, 1-5, doi: 10.1029/2012GL054231.

Brewer, P. G., G. T. F. Wong, M. P. Bacon, D. W. Spencer (1975), An oceanic calcium problem? *Earth and Planet. Sci. Lett., 26* (1), 81-87, doi: 10.1016/0012-821X(75)90179-X.

Cai, W.-J. X. Guo, C. A. Chen, M. Dai, L. Zhang, W. Zhai, S. E. Lohrenz, K. Yin, P. J. Harrison, Y. Wang (2008), A comparative overview of weathering intensity and HCO_3^- flux in the world's major rivers with emphasis on the Changjiang, Huanghe, Zhujiang (Pearl) and Mississippi Rivers, *Contental Shelf Res., 28*, 1538-1549.

Chen, C.-T. A. (2002), Shelf-vs. dissolution-generated alkalinity above the chemical lysocline, *Deep Sea Res. II, 49* (24–25), 5365-5375, doi: 10.1016/S0967-0645(02)00196-0.

Cooley, S. R., V. J. Coles, A. Subramaniam, and P. P. Yager (2007), Seasonal variations in the Amazon plume-related atmospheric carbon sink, *Global Biogeo. Chem. Cycles., 21* (3), GB3014, doi: 10.1029/2006GB002831

Craig, H., and K.K. Turekian (1980), The GEOSECS program 1976-1979, *Earth Planet. Sci.*

410 *Lett.*, *49*, 263-265, doi: 10.1016/j.bbr.2011.03.031.
411 Dai, A. and K. E. Trenberth (2002), Estimates of freshwater discharge from continents: latitudi-
412 nal and seasonal variations, *J. Hydrometeorology*, *3*, 660-687.
413 Dickson, A.G. (1981), An exact definition of total alkalinity and a procedure for the estimation
414 of alkalinity and total inorganic carbon from titation data, *Deep Sea Res. A, 28 (6)*, 609-623,
415 doi: 10.1016/0198-0149(81)90121-7.
416 Dickson, A. G. and F. J. Millero (1987), A comparison of the equilibrium constants for the
417 dissociation of carbonic acid in seawater media, *Deep-Sea Res. A*, *34*, 1733-1743.
418 Dieckmann, G.S., G. Nehrke, S. Papadimitriou, J. Göttlicher, R. Steininger, H. Kennedy, D.
419 Wolf-Gladrow, and D. N. Thomas (2008), Calcium carbonate as ikaite crystals in Antarctic
420 sea ice, *Geophys. Res. Lett. , 35*, LO8051, doi:10.1029/2008GL033540.
421 Feely, R. A., C. L. Sabine, K. Lee, F. J. Millero, M. F. Lamb, D. Greeley, J. L. Bullister, R. M.
422 Key, T. H. Peng, and A. Kozyr (2002), In situ calcium carbonate dissolution in the Pacific
423 Ocean, *Global Biogeochem. Cycles, 16*, 1144, doi: 10.1029/2002GB001866.
424 Feely, R. A., R.H. Byrne, J. G. Acker, P. R. Betzer, C. A. Chen, J. F. Gendron, and M. F. Lamb
425 (1988), Winter-summer variations of calcite and aragonite saturation in the northeast
426 Pacific. *Mar. Chem.* 25, *3*, 227-241.
427 Fofonof, N. P., and R. C. Millard (1983), Algorithms for computations of fundamental properties
428 of seawater. UNESCO Technical Papers in Marine Science No. 44, 53 pp.
429 Gascard, J. C., G. Raisbeck, S. Sequeira, F. Yiou, and K. Mork (2004), Correction to 'The
430 Norwegian Atlantic Current in the Lofoten basin inferred from hydrological and tracer
431 data(I-129) and its interaction with the Norwegian Coastal Current'. *Geophys. Res.*
432 *Lett.*, *31*(8).

433 Gascard, J. C., G. Raisbeck, S. Sequeira, F. Yiou, and K. Mork (2004), Correction to
434 2003GL01803, *Geophys. Res. Lett., 31*, L08302, doi:10.1029/2004GL020006, 2004.
435 Gevirtz, J. L., and G. M. Friedman (1966), Deep-Sea carbonate sediments of the Red Sea and
436 their implications on marine lithification, *J. Sed. Petrol.*, *36*, 143-151.
437 Gruber, N., and J. L. Sarmiento (1997), Global patterns of marine nitrogen fixation and
438 denitrification, *Global Biogeochemical Cycles*, *11*(2), 235-266.
439 Hales, B. (2003), Respiration, dissolution, and the lysocline. *Paleoceanogr.*, *18*(4), 1099.
440 Hales, B., and S. Emerson (1997), Calcite dissolution in sediments of the Ceara Rise: In situ
441 measurements of porewater O2, pH, and CO2 (aq). *Geochim. Cosmochim. Acta*, *61*(3), 501-
442 514.
443 Honjo, S., S. J. Manganini, R. A. Krishfield, and R. Francois (2008), Particulate organic carbon
444 fluxes to the ocean interior and factors controlling the biological pump: A synthesis of global
445 sediment trap programs since 1983, *Prog. Oceanogr.*, *76*(3), 217-285.
446 Ilyina, T. R. E. Zeebe, E. Maier-Reimer, and C. Heinze (2009), Early detection of ocean
447 acidification effects on marine calcification, *Global Biogeochem. Cycles, 23*, GB1008, doi:
448 10.1029/2008GB003278.
449 Jiang, Z. P., T. Tyrrell, D.J. Hydes, M. Dai, and S.E. Hartman (2014), Variability of alkalinity
450 and the alkalinity-salinity relationship in the tropical and subtropical surface ocean. *Global*
451 *Biogeochem. Cycles*, *28*(7), 729-742, doi: 10.1002/2013GB004678.
452 Jones, E. P., L. G. Anderson, S. Jutterström, L. Mintrop, and J. H. Swift (2008), Pacific
453 freshwater, river water and sea ice meltwater across Arctic Ocean basins: Results from the
454 2005 Beringia Expedition, *J. Geophys. Res. Oceans*, *113*(C8).
455 Kanamori, S. and H. Ikegami (1982), Calcium-alkalinity relationship in the North Pacific, *J.*

456 *Oceanogr., 38*, 57-62.

457 Kaushal, S. S., G. E. Likens, R. M. Utz, M. L. Pace, M. Grese, and M. Yepsen (2013), Increased
458 river alkalinization in the Eastern U.S., *Envi. Sci. Tech., 47*, 10302-10311, doi:
459 10.1021/es401046s.

460 Key, R. M., A. Kozyr, C. L. Sabine, K. Lee, R. Wanninkhof, J. L. Bullister, R. A. Feely, F. J.
461 Millero, C. Mordy, and T. H. Peng (2004), A global ocean carbon climatology: Results from
462 Global Data Analysis Project (GLODAP), *Global Biogeochem. Cycles, 18*, GB4031, doi:
463 10.1029/2004GB002247.

464 Key, R. M., T. Tanhua, A. Olsen, M. Hoppema, S. Jutterström, C. Schirnick, S. van Heuven, X.
465 Lin, D. Wallace and L. Mintrop (2009), The CARINA data synthesis project: Introduction
466 and overview, *Earth Sys. Sci. Data, 2(1),* 579-624.

467 Khatiwala, S., M. Visbeck, and M. A. Cane, (2005), Accelerated simulation of passive tracers in
468 ocean circulation models, *Ocean Modelling*, *9*(1), 51-69.

469 Khatiwala, S. (2007), A computational framework for simulation of biogeochemical tracers in
470 the ocean, *Global Biogeochemical Cycles*, *21*(3), GB3001.

471 Mehrbach, C., C. H. Culberson, J. E. Hawley, and R. M. Pytkowicz (1973), Measurement of the
472 apparent dissociation constants of carbonic acid in seawater at atmospheric pressure, *Limnol.*
473 *Oceanogr., 18*, 897-907.

474 Millero, F. J., K. Lee, and M. Roche, (1998), Distribution of alkalinity in the surface waters of
475 the major oceans, *Marine Chemistry, 60*, 111-130.

476 Milliman, J. D., D. A. Ross, and T. L. Ku (1969), Precipitation and lithification of deep-sea
477 carbonates in the Red Sea, *J. Sed Res.*, *39*(2), 724-736.

478 Moore, W. S. (2010), The effect of submarine groundwater discharge on the ocean. *Marine Sci.*,

2, 59-88, doi: 10.1146/annurev-marine-120308-081019

Moore, W. S., J. L. Sarmiento, and R. M. Key (1986), Tracing the Amazon component of surface Atlantic water using ^{228}Ra, salinity, and silica, *J. Geophys. Res.*, *91* (*C2*), 2574-2580.

Robbins, P. E. (2001), Oceanic carbon transport carried by freshwater divergence: Are salinity normalizations useful?. *J. Geophys. Res*, *106*(C12), 30939-30.

Sarmiento, J. L., J. Dunne, A. Gnanadesikan, R.M. Key, K. Matsumoto, R. Slater (2002), A new estimate of the CaCO3 to organic carbon export ratio. *Global Biogeochem. Cy.*, *16*(4), 1107.

Sarmiento, J. L., N. Gruber, M. A. Brzezinski, and J. P. Dunne (2004), High-latitude controls of thermocline nutrients and low latitude biological productivity. *Nature*, *427*(6969), 56-60.

Silverman, J. B. Lazar, and J. Erez (2007), Effect of aragonite saturation, temperature, and nutrients on the community calcification rate of a coral reef, *J. Geophys. Res.*, *112*, CO05004, DOI: 10.1029/2006JC003770.

Suzuki, T., M. Ishii, M. Aoyama, J. R. Christian, K. Enyo, T. Kawano, R. M. Key, N. Kosugi, A. Kozyr, L. A. Miller, A. Murata, T. Nakano, T. Ono, T. Saino, K. Sasaki, D. Sasano, Y. Takatani, M. Wakita and C. Sabine (2013), PACIFICA Data Synthesis Project. ORNL/CDIAC-159, NDP-092. Carbon Dioxide Information Analysis Center, Oak Ridge National Laboratory, U.S. Department of Energy, Oak Ridge, Tennessee. doi:10.3334/CDIAC/OTG.PACIFICA_NDP092.

Takahashi, T., S. C. Sutherland, R. Wanninkhof, C. Sweeney, R. A. Feely, D. W. Chipman, B. Hales, G. Friederich, F. Chavez, C. Sabine, A. Watson, D. C. E. Bakker, U. Schuster, N. Metzl, H. Yoshikawa-Inoue, M. Ishii, T. Midorikawa, Y. Nojiri, A. Körtzinger, T. Steinhoff, M. Hoppema, J. Olafsson, T. S. Arnarson, B. Tilbrook, T. Johannessen, A. Olsen, R. Bellerby, C. S. Wong, B. Delille, N. R. Bates, and J. W. deBarr, (2009), Climatological mean

and decadal change in surface ocean pCO_2, and net sea–air CO_2 flux over the global oceans, *Deep Sea Res. II*, *56*(8), 554-577.

Thomas, H., Y. Bozec, H. J. De Baar, K. Elkalay, M. Frankignoulle, L. S. Schiettecatte, G. Kattner, and A. V. Borges (2005), The carbon budget of the North Sea. *Biogeosci.*, *2*(1), 87-96.

Tynan, E., T. Tyrrell, and E. P. Achterberg (2014), Controls on the seasonal variability of calcium carbonate saturation states in the Atlantic gateway to the Arctic Ocean. *Mar. Chem.* 158 (2014) 1-9. doi: 10.1016/j.marchem.2013.10.010

van Heuven, S., D. Pierrot, E. Lewis, and D. Wallace (2009), MATLAB Program developed for CO_2 system calculations, *ORNL/CDIAC-105b, Carbon Dioxide Information Analysis Center, Oak Ridge National Laboratory, US Department of Energy, Oak Ridge, Tennessee*.

Velo, A., F. F. Perez, P. Brown, T. Tanhua, U. Schuster, and R. M. Key (2009), CARINA alkalinity data in the Atlantic Ocean, *Earth Syst. Sci. Data*, *1*, 45-61, doi:10.5194/essd-1-45-2009.

de Villiers, S. (1998), Excess dissolved calcium in the ocean: a hydrothermal hypothesis, *Earth and Plan. Sci. Lett.*, *164(3-4)*, 624-641.

Wolery, T. J., and N. H. Sleep (1988), Interactions of geochemical cycles with the mantle. In: Gregor, C. B., R. M. Garrels, F. T. Mackenzie, and J. B. Maynard (eds) Chemical cycles in the evolution of the earth. Wiley, New York, 77-103.

Wolf-Gladrow, D. A., R. E. Zeebe, C. Klaas, A. Körtzinger, and A. G. Dickson (2007), Total alkalinity: The explicit conservative expression and its application to biogeochemical processes. *Marine chemistry*, *106*(1), 287-300.

Yamamoto-Kawai, M., F. A. McLaughlin, E. C. Carmack, S. Nishino, and K. Shimada (2009),

525 Aragonite undersaturation in the Arctic Ocean; effects of ocean acidification and sea ice
526 melt, *Science, 326*, 1098, doi:10.1126/science.1174190.

527 **Appendix A: Definition of the process importance metric M**

528 In simplest terms, our metric is the product of the calcite saturation sensitivity to a
529 process and the variability of the net influence of the process globally. The difficulty in this
530 calculation lies in quantifying the "net influence of a process." We first show how we change
531 coordinates so we can use reference tracers as a proxy measurement for these net influences.

532 Our metric for Ω_C variability resulting from the *i*th process is expressed as M_i:

533 $$M_i = \sigma_{P_i} \left| \frac{\partial \Omega_C}{\partial P_i} \right| \quad \text{(A1)}$$

534 where P_i is an abstract variable representing the net process influence (that we will later factor
535 out), and $\frac{\partial \Omega_C}{\partial P_i}$ is the calcite saturation sensitivity to the process. We expand $\frac{\partial \Omega_C}{\partial P_i}$ using the
536 chain rule to include a term for Ω_C sensitivity to changes in the reference tracer R_i (see section 4)
537 and a term $\frac{\partial R_i}{\partial P_i}$ representing changes in R_i resulting from the *i*th process:

538 $$\frac{\partial \Omega_C}{\partial P_i} = \frac{\partial \Omega_C}{\partial R_i} \frac{\partial R_i}{\partial P_i} \quad \text{(A2)}$$

539 In practice, we calculate Ω_C as a function of $j = 7$ properties: (1) pressure, (2)
540 temperature, (3) salinity, (4) phosphate, (5) silicate, (6) A_T, and (7) C_T for mean seawater and
541 pCO_2 for surface seawater, so we use the chain rule again to expand the $\frac{\partial \Omega_C}{\partial R_i}$ terms as follows:

542 $$\frac{\partial \Omega_C}{\partial R_i} = \sum_{j=1}^{7} \frac{\partial \Omega_C}{\partial X_j} \frac{\partial X_{j,i}}{\partial R_i} \quad \text{(A3)}$$

543 Here, the $\frac{\partial X_{j,i}}{\partial R_i}$ are assumed terms (assumptions detailed shortly) that relate the effect of the *i*th

process on the *j*th property to the effect of the process on R_i, and the $\frac{\partial \Omega}{\partial X_j}$ terms reflect calcite saturation sensitivity to changes in the *j* properties used to calculate it.

We make assumptions regarding the $\frac{\partial X_{j,i}}{\partial X_{\mathrm{R}}}$ terms: we relate changes in temperature from sinking or shoaling to changes in pressure using the potential temperature (θ) routines of Fofonoff and Millard (1983); we assume freshwater cycling linearly concentrates A_{T}, C_{T}, phosphate, and silicate by the same ratio that it changes salinity; we relate C_{T}, phosphate, and A_{T} changes from organic matter formation to changes in phosphate using the remineralization ratios found by Anderson and Sarmiento (1994) and the empirical relationship of Kanamori and Ikegami (1982); we also use Kanamori and Ikegami (1982)'s constant to relate changes in A_{T} from nitrogen fixation and denitrification to changes in N* from these processes; and we assume that an increase in A_{T} from calcium carbonate dissolution equals the *Alk** increase, and that the corresponding increase in C_{T} equals half of this *Alk** increase. We neglect any changes in C_{T} from denitrification and nitrogen fixation because these changes are better thought of as organic matter cycling occurring alongside nitrogen cycling.

We estimate $\frac{\partial \Omega}{\partial X_j}$ property sensitivity terms as the differences between Ω_{C} calculated before and after augmenting *j*th property by 1 unit. Ω_{C} is calculated with the MATLAB CO2SYS routines written by van Heuven et al. (2009) using the carbonate system equilibrium constants of Mehrbach et al. (1973), as refit by Dickson and Millero (1987). Seawater $p\mathrm{CO}_2$ is used in place of C_{T} for the surface seawater calculations (when $j = 7$) to calculate the change in Ω_{C} that remains after the surface seawater is allowed to equilibrate with the atmosphere.

564 We assume that the distributions of our R_i reference properties are linearly related to the

565 P_i net activities of their associated processes. This assumption implies:

566 $$\sigma_P = \sigma_{R_i} \left| \frac{\partial P_i}{\partial R_i} \right| \quad \text{(A4)}$$

567 We can then substitute Eq. (A3) into Eq. (A2), and substitute this combined equation for $\frac{\partial \Omega_C}{\partial P_i}$

568 and (A4) into Eq. (A1). We then and cancel the $\frac{\partial P_i}{\partial R_i}$ and $\frac{\partial R_i}{\partial P_i}$ terms to obtain:

569 $$M_i = \sigma_{R_i} \left| \sum_{j=1}^{7} \frac{\partial \Omega_C}{\partial X_j} \frac{\partial X_{j,i}}{\partial R_i} \right| \quad \text{(A5)}$$

570 We then define our saturation sensitivity S_{R_i} as:

571 $$S_{R_i} = \left| \sum_{j=1}^{7} \frac{\partial \Omega_C}{\partial X_j} \frac{\partial X_{j,i}}{\partial R_i} \right| \quad \text{(A6)}$$

572 where S_{R_i} is the saturation sensitivity to a change in the *i*th process scaled to a unit change in the

573 reference variable for that process. We can then substitute Eq. (A6) into Eq. (A5) to obtain Eq.

574 6. We use Eqn. (A6) to define S_{R_i} and Eqn. 6 to calculate *M*. We provide the $\frac{\partial \Omega_C}{\partial X_j}$ and $\frac{\partial X_{j,i}}{\partial R_i}$

575 values we use to estimate S_{R_i} for atmospherically isolated seawater from all depths in Table A1

576 and for well-equilibrated surface seawater in Table A3. We perform a sample *I* and *M*

577 calculation in Supplementary Materials document SE.

578 We use a Monte Carlo analysis to estimate variability and uncertainty in our metric *M*

579 and our percent relative process importance *I* calculations. We calculate the standard deviations,

580 σ_M and σ_I, of pools of 1000 *M* and *I* estimates calculated after adjusting the seawater properties

581 X_i with a normally-distributed perturbation with a standard deviation equal to the property

582 standard deviation from the gridded dataset. We find $\frac{\sigma_I}{I}$ is typically much smaller than $\frac{\sigma_M}{M}$.

583 This is because calcite saturation sensitivity is typically proportional to the calcite saturation

584 itself, so individual Monte Carlo *M* estimates vary with the initial calcite saturation and one

585 another. Our σ_M estimates are therefore better thought of as measures of the ranges of

586 sensitivities found in the modern ocean, while σ_I represent variability in the relative importance

587 of processes. We provide σ_M and σ_I for atmospherically isolated seawater globally in Table

588 A2, and for well-equilibrated surface seawater in Table A4.

589

590

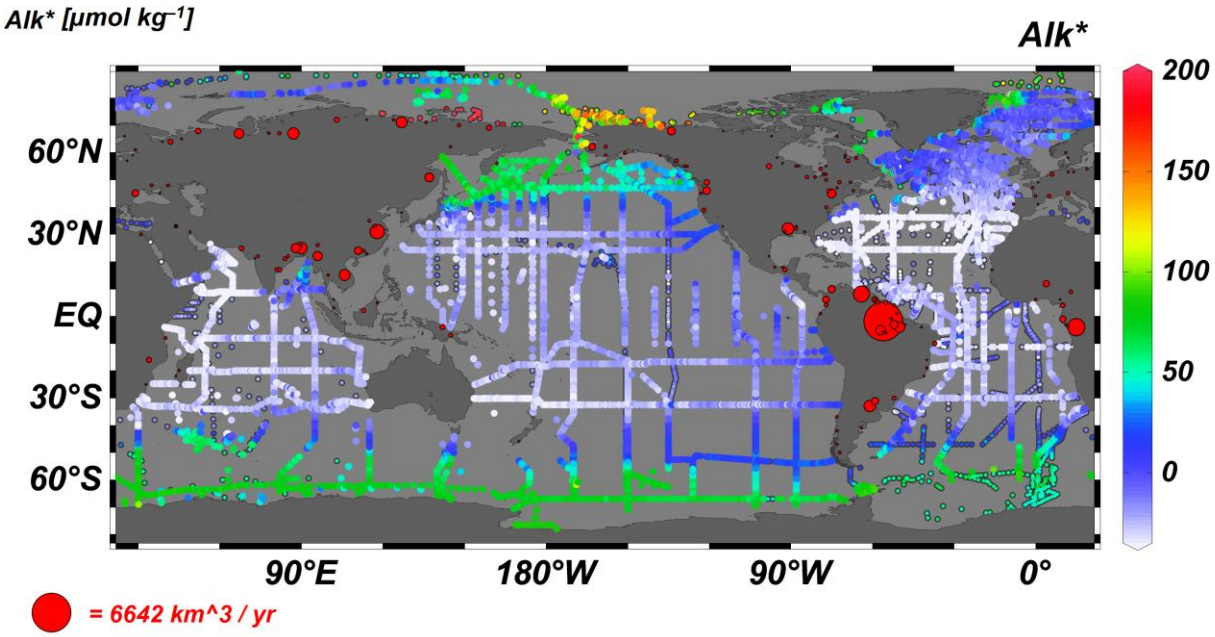

Figure 1. A map of station locations at which we use measurements to estimate *Alk** (in µmol kg^{-1}). Dot color indicates surface *Alk**. Points with black borders indicate that either A_T was measured prior to 1992 (i.e. before reference materials were commonly used) or that no nitrate value was reported (in which case a nitrate concentration of 5 µmol kg^{-1} is assumed). Red dots on land indicate the mouth locations and mean annual discharge volumes (indicated by dot size) of 200 large rivers, as given by Dai and Trenberth (2002).

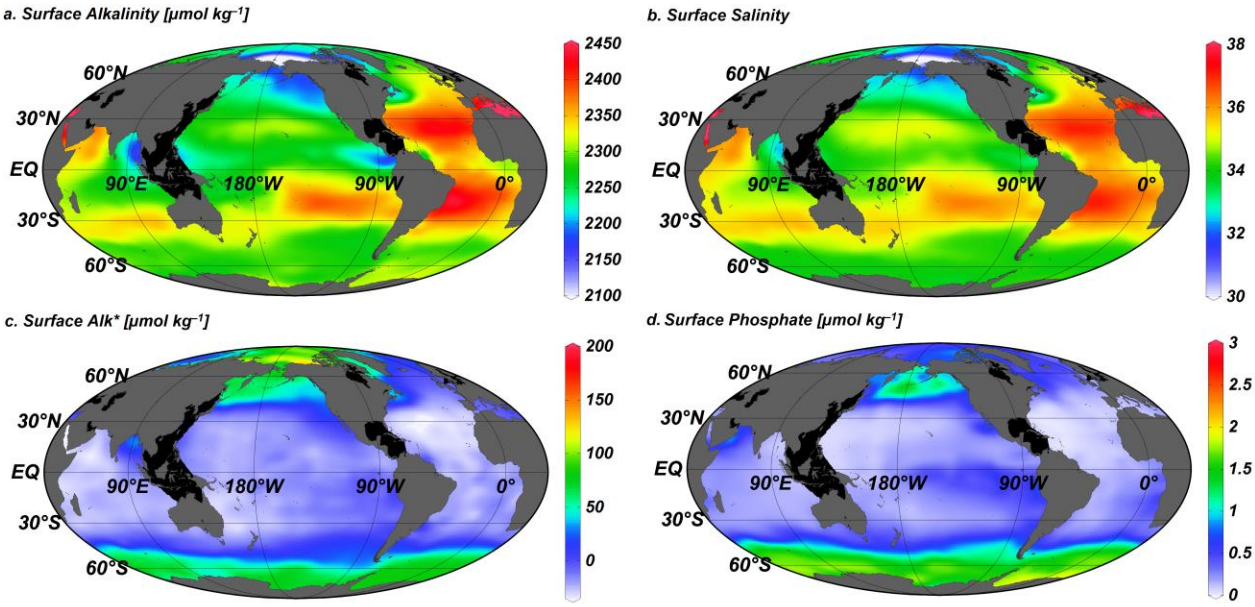

Figure 2. Global (a) total alkalinity A_T, (b) salinity, (c) *Alk**, and (d) phosphate distributions at the surface (10 m depth surface) from our gridded CARINA, PACIFICA, and GLODAP bottle data product. Areas with exceptionally poor coverage in the data used to produce the gridded product are blacked out.

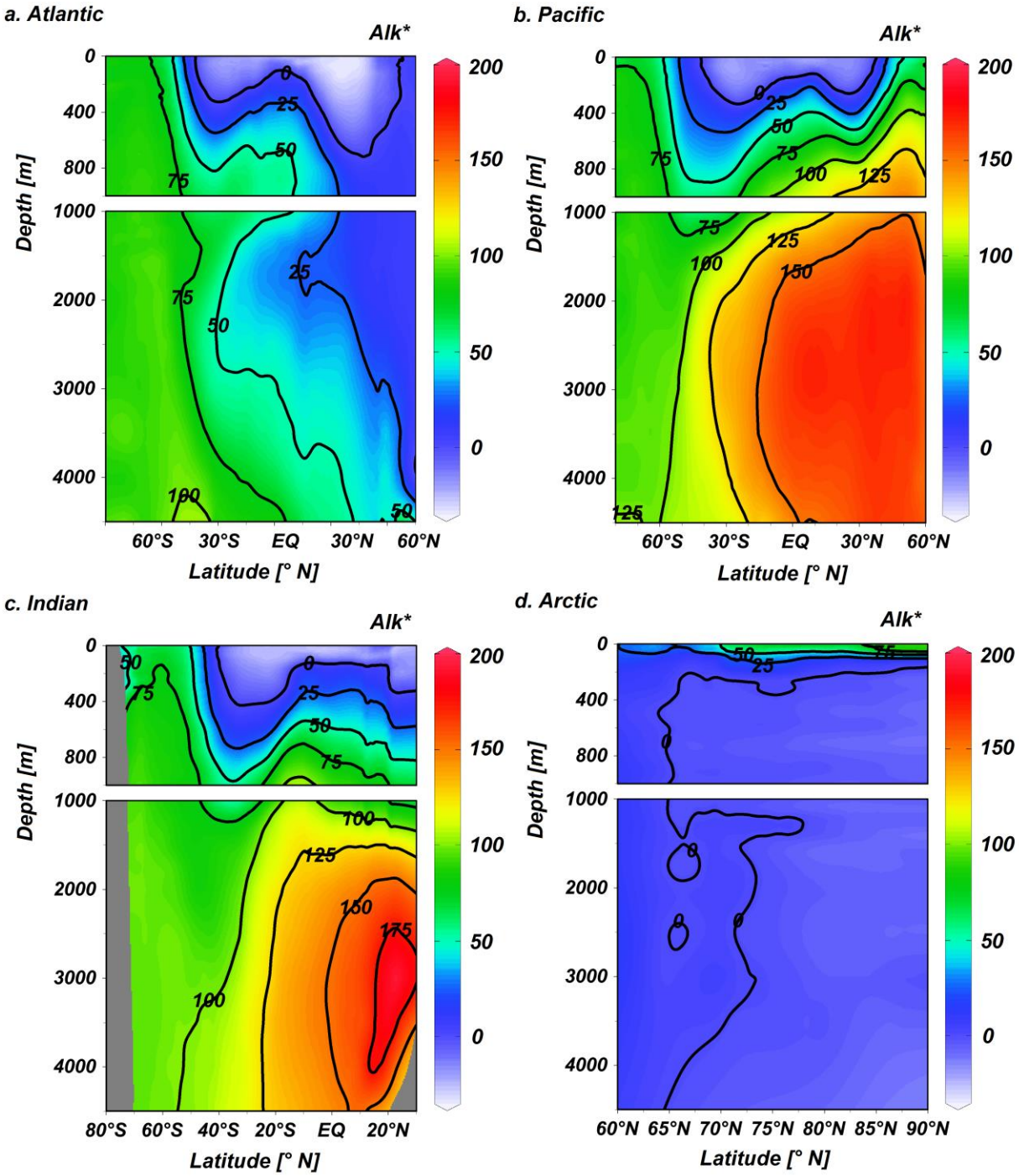

Figure 3. Zonal mean gridded *Alk** (in µmol kg^{-1}) in the (a) Atlantic, (b) Pacific, (c) Indian, and (d) the Arctic oceans plotted against latitude and depth.

603

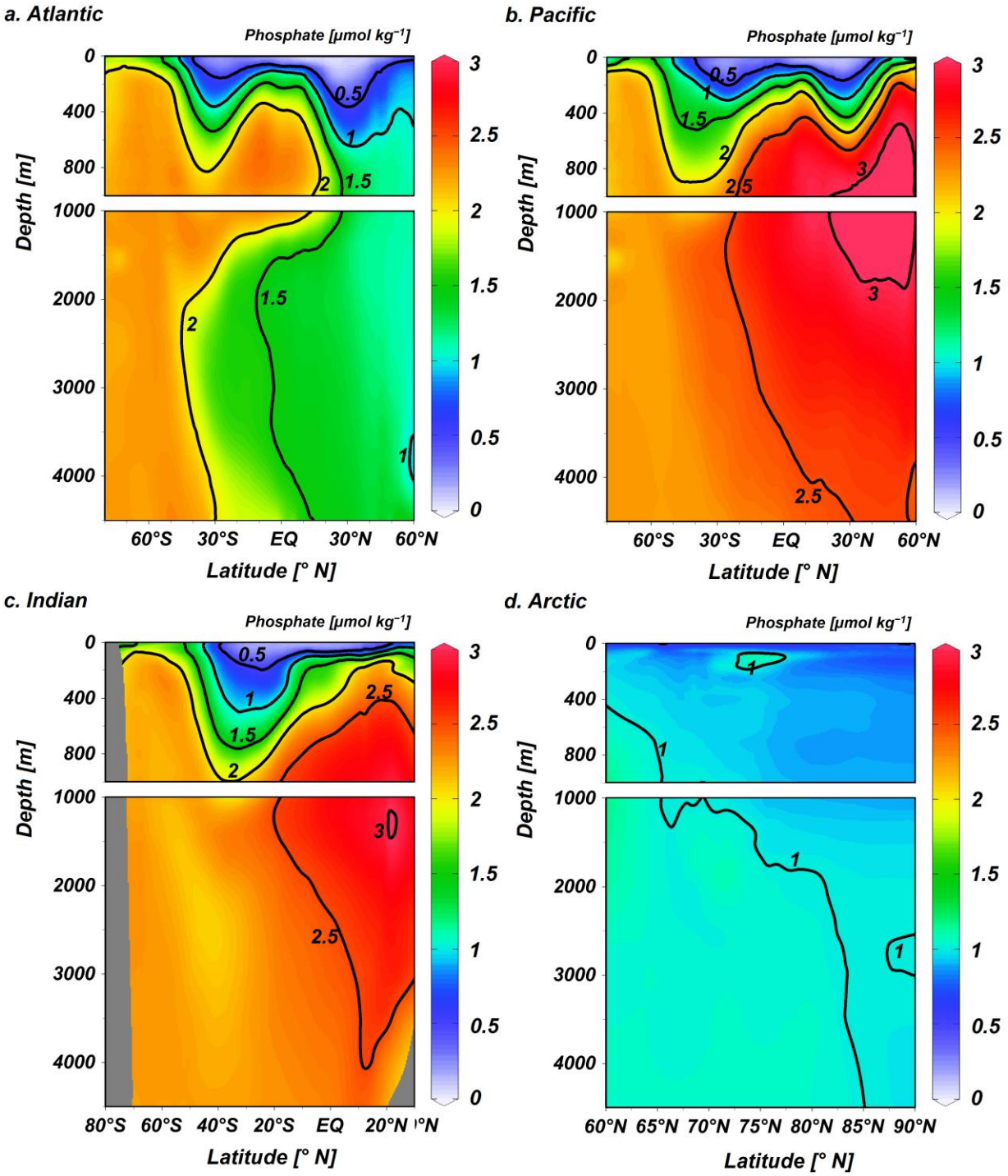

Figure 4. Zonal mean gridded phosphate (in µmol kg^{-1}) in the (a) Atlantic, (b) Pacific, (c) Indian, and (d) the Arctic oceans plotted against latitude and depth.

604

605

606

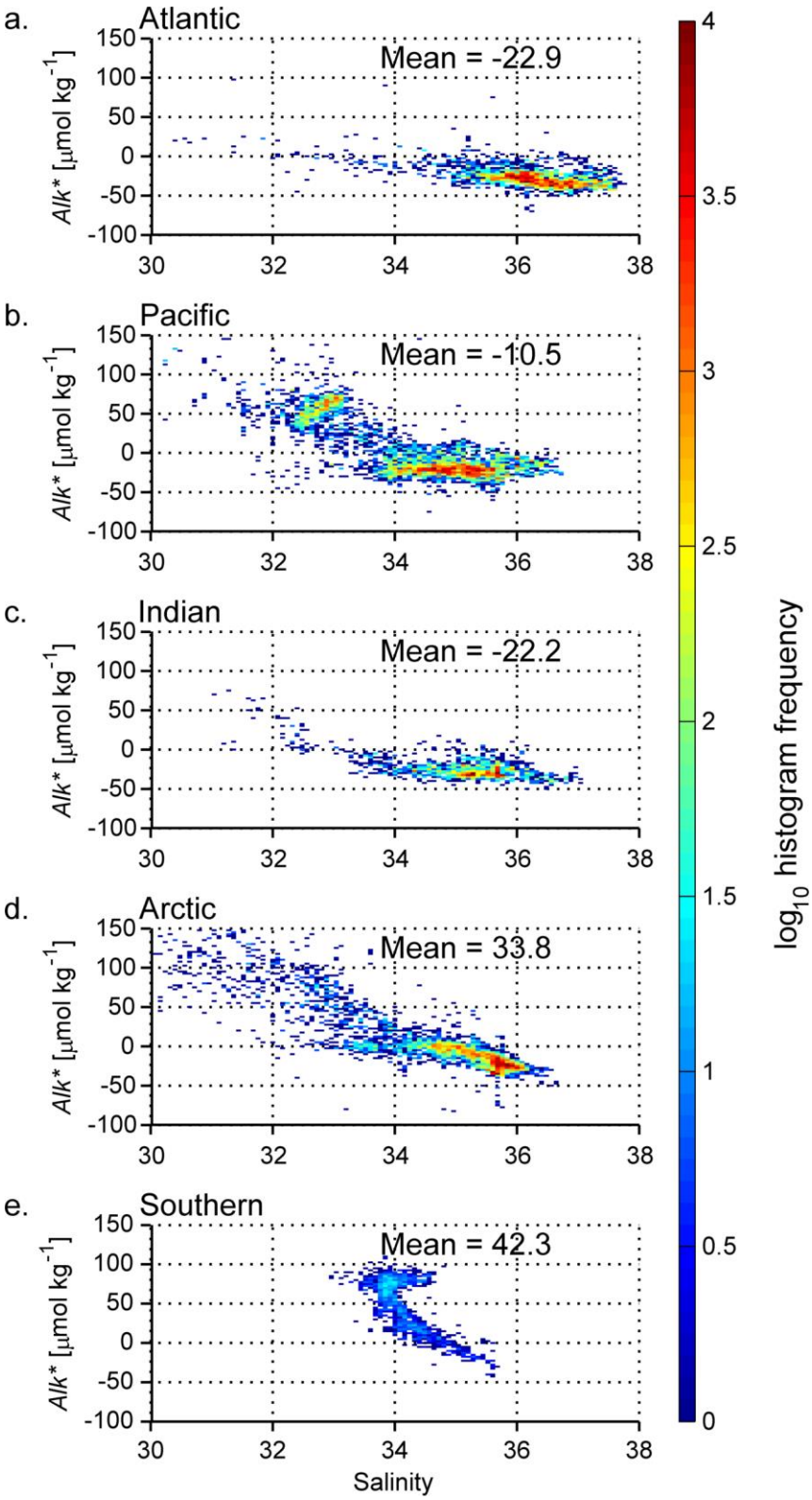

Figure 5. 2-D histograms indicating the log (base 10) of the number of measurements that fall within bins of *Alk** vs. salinity with color. Data are limited to the top 50 m of the (a) Atlantic, (b) Pacific, (c) Indian, (d) Arctic, and (e) Southern Oceans. Where basins connect, the boundary between the Atlantic and the Arctic oceans is 40°N, between the Atlantic and the Indian is 20° E,

between the Indian and the Pacific is 131° E, between the Pacific and the Atlantic is 70° W, and between the Southern Ocean and the other oceans is 40°S.
607

608

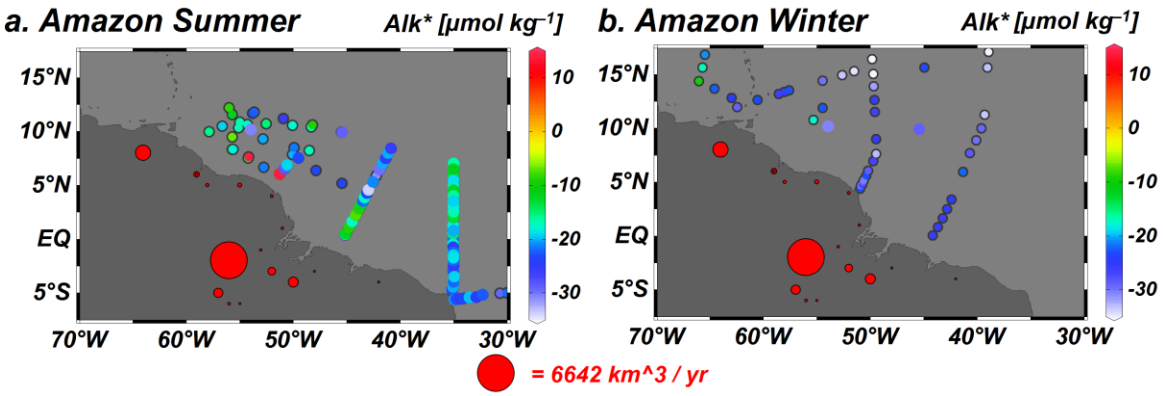

Figure 6. *Alk** (in µmol kg^{-1}) in top 50 m of the ocean near the Amazon River outflow plotted in color, though with a narrower color scale than is used for all other plots. Panel (a) is limited to data collected in November through January, and in panel (b) is limited to measurements from May through July. Points with black borders indicate that either the A_T was measured prior to 1992 (before reference materials were commonly used) or that no nitrate value was reported (in which case a nitrate concentration of 5 µmol kg^{-1} is assumed). Red dots on land indicate the mouth locations and mean annual discharge volumes (indicated by dot size) of large rivers, as given by Dai and Trenberth (2002).

609

610

611

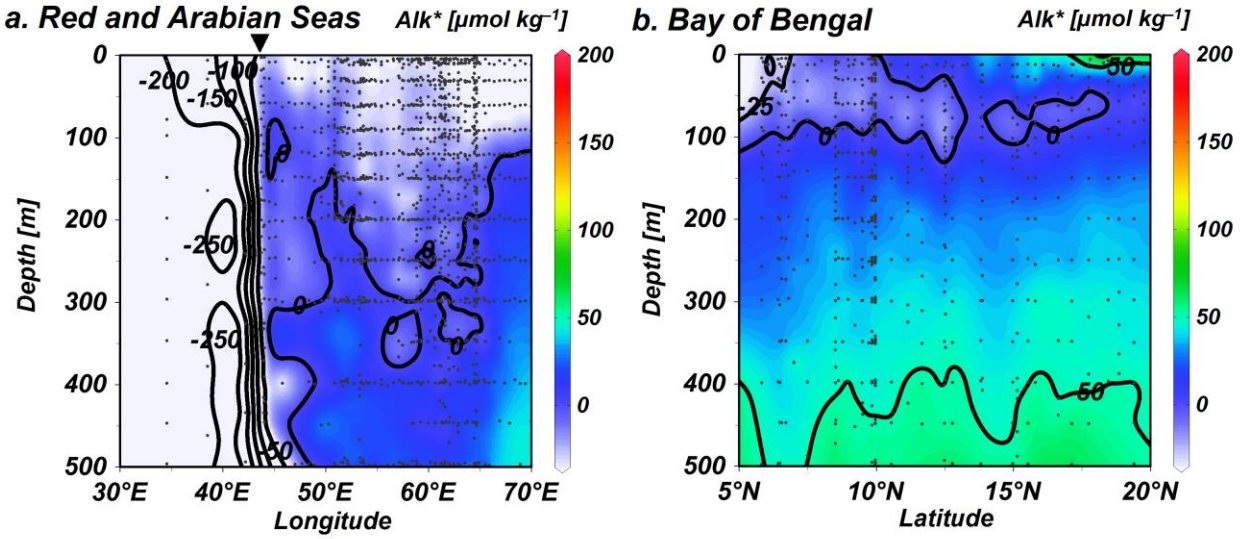

Figure 7. *Alk** distributions (in µmol kg^{-1}) (a) between 5° and 30°N in the Red and Arabian Seas shown against longitude, and (b) between 75° and 100° E in the Bay of Bengal plotted against latitude. Small black dots indicate where data is present. The inverted triangle above (a) indicates the longitude of the mouth of the Red Sea.

612

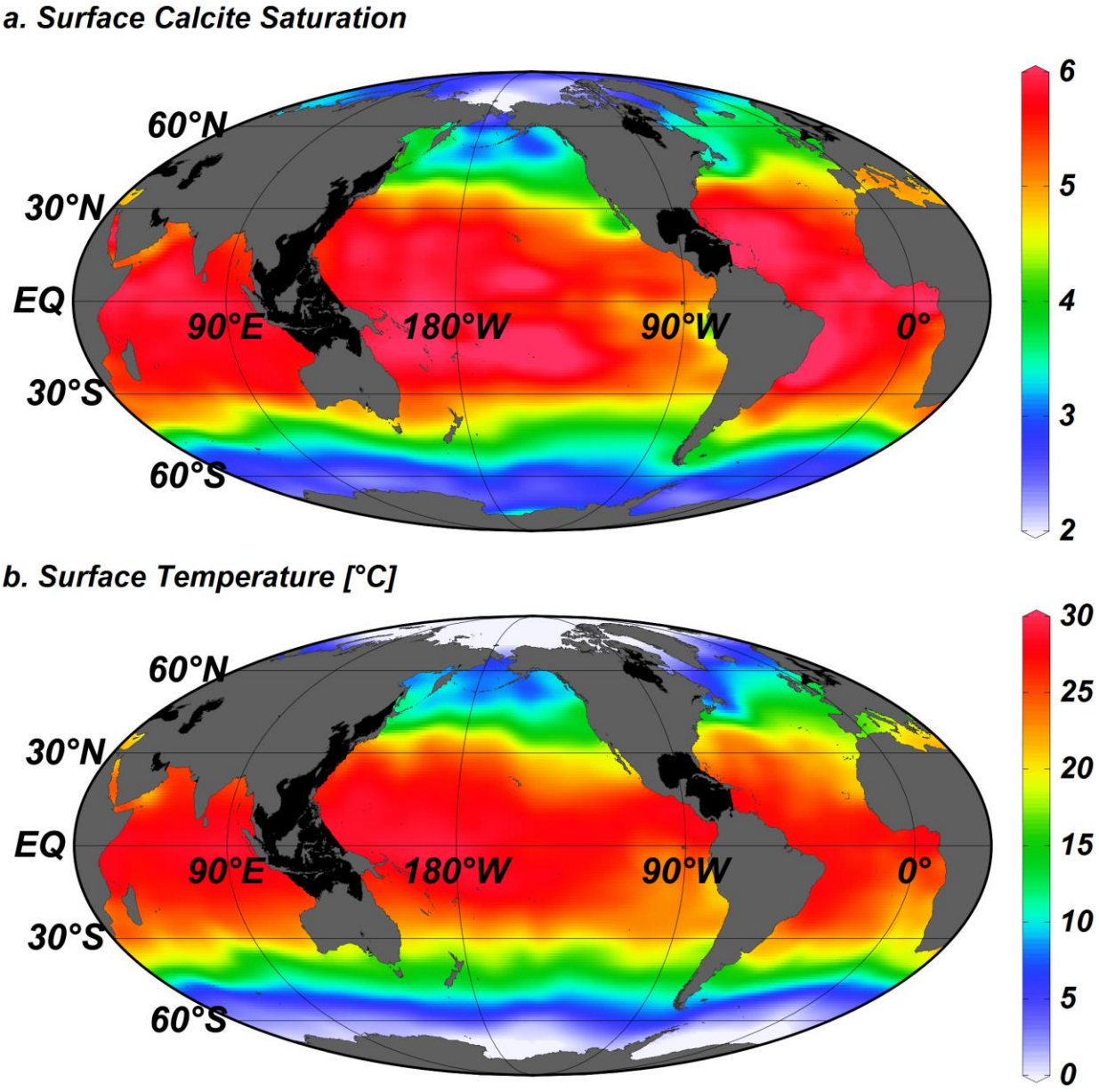

Figure 8. Gridded global (a) calcite saturation, and (b) temperature at the surface (10 m depth surface) of our gridded CARINA, PACIFICA, and GLODAP bottle data product. Areas with exceptionally poor coverage in the data used to produce the gridded product are blacked out.

613

614

615

616

617

618

Table 1. Metric estimates M_i, relative process importance percentages I_i, calcite saturation sensitivities S_{R_i} to unit changes in the R_i reference properties, and reference property standard deviations σ_{R_i} for the i = 6 processes in atmospherically isolated mean seawater from all ocean depths. See Appendix A for details on how these terms are estimated and explanation of how M_i and I_i uncertainties are obtained.

Process	i	R_i	S_{R_i}	σ_{R_i}	M_i	I_i
Carbonate cycling	1	*Alk**	0.0043	53.5 µmol/kg	0.23	17%
Org. matter cycling	2	Phosphate	−0.0069	0.60 µmol/kg	0.66	48%
Freshwater cycling	3	Salinity	0.032	0.27	0.011	0.78%
Sinking / shoaling	4	Pressure	−0.00028	1411 db	0.4	28%
Warming / cooling	5	Temp.	0.014	4.20 °C	0.06	4%
Denit./nit. fix.	6	N*	−0.010	1.6 µmol/kg	0.017	1.2%

619

620

621

Table 2. Metric estimates M_i, relative process importance percentages I_i, calcite saturation sensitivities S_{R_i} to unit changes in the R_i reference properties, and reference property standard deviations σ_{I_i} for the i = 6 processes in well-equilibrated surface seawater. See Appendix A for details on how these terms are estimated and explanation of how M_i and I_i uncertainties are obtained.

Process	i	R_i	S_{R_i}	σ_{R_i}	M_i	I_i
Carbonate cycling	1	*Alk**	0.0034	36.9 µmol/kg	0.13	7.8%
Org. matter cycling	2	Phosphate	−0.0045	0.51 µmol/kg	0.037	2.3%
Freshwater cycling	3	Salinity	0.20	0.86	0.22	13.2%
Sinking / shoaling	4	Pressure	−0.00083	15 db	0.011	0.70%
Warming / cooling	5	Temp.	0.14	8.8 °C	1.2	76%
Denit ./ nit. fix.	6	N*	−0.0043	1.5 µmol/kg	0.006	0.40%
pCO_2 disequilibria	†	pCO_2	−0.0086	27 µatm*	0.23	†

* standard deviation of the Takahashi et al. (2009) revised global monthly pCO_2 climatology

† the M value for disequilibria is only calculated to test our assumption of surface seawater air-sea equilibration, and is omitted from calculations of I_i for comparison with Table 1.

622

623

624

Table A1. $\frac{\partial \Omega_C}{\partial X_j}$ (bold text) and $\frac{\partial X_{j,i}}{\partial R_i}$ (italic text) terms used in Eq. (A5) for atmospherically isolated mean seawater from all ocean depths. These terms are specific to the $j = 7$ (columns) properties we use to calculate Ω_C and $i = 6$ (rows) processes we consider. Units for $\frac{\partial \Omega_C}{\partial X_j}$ are the inverse of the listed X_j units. Units for $\frac{\partial X_{j,i}}{\partial R_i}$ are the X_j units divided by the R_i units given in Table 1.

Properties		Pressure	Temp	Salinity	Phos.	Silicate	A_T	C_T
X_j *units*		db	°C		µmol/kg	µmol/kg	µmol/kg	µmol/kg
j		1	2	3	4	5	6	7
Mean seawater values		2235	3.7	34.71	2.15	49.0	2362	2254
Process	*i*	**–0.00028**	**0.014**	**–0.011**	**–0.0085**	**–0.00012**	**0.0082**	**–0.0079**
Carbonate cycling	1	-	-	-	-	-	*1*	*0.5*
Org. matter cycling	2	-	-	-	*1*	-	*–20.16*	*117*
Freshwater cycling	3	-	-	*1*	*0.062*	*1.4*	*68*	*65*
Sinking / shoaling	4	*1*	*0.00010*	-	-	-	-	-
Warming / cooling	5	-	*1*	-	-	-	-	-
Denit ./ nit. fix.	6	-	-	-	-	-	*–1.26*	-

625

626

627

628

Table A2. Monte Carlo derived estimates for M_i variability (σ_{M_i}) and I_i variability (σ_{I_i}) for atmospherically-isolated mean seawater from all ocean depths.

Process	i	σ_{M_i}	σ_{I_i}
Carbonate cycling	1	0.09	1%
Org. matter cycling	2	0.2	3%
Freshwater cycling	3	0.006	0.08%
Sinking / shoaling	4	0.2	5%
Warming / cooling	5	0.02	2%
Denit. / nit. fix.	6	0.006	0.1%

629

630

631

Table A3. $\frac{\partial \Omega_C}{\partial X_j}$ (bold text) and $\frac{\partial X_{j,i}}{\partial R_i}$ (italic text) terms used in Eq. (A5) for well-equilibrated surface seawater. These terms are specific to the j = 7 (columns) properties we use to calculate Ω_C and i = 6 (rows) processes we consider. Units for $\frac{\partial \Omega_C}{\partial X_j}$ are the inverse of the listed X_j units. Units for $\frac{\partial X_{j,i}}{\partial R_i}$ are the X_j units divided by the R_i units given in Table 2.

Properties		Pressure	Temp	Salinity	Phos.	Silicate	A_T	pCO_2
units		db	°C		µmol/kg	µmol/kg	µmol/kg	µatm
j		1	2	3	4	5	6	7
Mean seawater values		25	18.3	34.82	0.51	2.5	2305	350
Process	*i*	**–0.00084**	**0.14**	**–0.022**	**–0.0038**	**–0.00013**	**0.0034**	**–0.0086**
Carbonate cycling	1	-	-	-	-	-	*1*	-
Org. matter cycling	2	-	-	-	*1*	-	*–20.16*	-
Freshwater cycling	3	-	-	*1*	*0.015*	*0.072*	*65.9*	-
Sinking / shoaling	4	*1*	*0.00010*	-	-	-	-	-
Warming / cooling	5	-	*1*	-	-	-	-	-
Denit./nit. fix.	6	-	-	-	-	-	*–1.26*	-

632

633

Table A4. Monte Carlo derived estimates for M_i variability (σ_{M_i}) and I_i variability (σ_{I_i}) for well-equilibrated surface seawater.

Process	i	σ_{M_i}	σ_{I_i}
Carbonate cycling	1	0.03	0.8%
Org. matter cycling	2	0.01	0.2%
Freshwater cycling	3	0.04	0.5%
Sinking / shoaling	4	0.001	0.03%
Warming / cooling	5	0.2	1%
Denit. / nit. fix	6	0.002	0.04%
pCO$_2$ disequilibria	†	0.05	†

† disequilibria are included only as a test of our assumption of surface seawater air-sea equilibration, so these M_i values are omitted from calculations of I

634

635

636